Case Studies in Thermal Engineering 64 (2024) 105438

Contents lists available at ScienceDirect

Case Studies in Thermal Engineering

journal homepage: www.elsevier.com/locate/csite

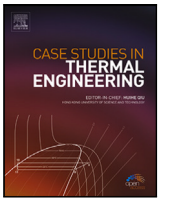

Direct forcing immersed boundary method for electro-thermo-buoyant flows in enclosures

Mukesh Kumar *, Yohay Mayan, Yuri Feldman

Department of Mechanical Eng., Ben-Gurion University of the Negev, Beer-Sheva, Israel

HIGHLIGHTS

- Electro-thermo-buoyant flows.
- Immersed boundary (IB) method.
- IB-FV solver.

ARTICLE INFO

Keywords:
Electro-thermo-buoyant flows
Immersed boundary (IB) method
IB-FV solver

ABSTRACT

This study investigates electro-hydrodynamic (EHD) and electro-thermo-hydrodynamic (ETHD) phenomena in dielectric liquids, and focusses on charge injection as a source of unipolar charges. The studied configuration consists of a hot spherical electrode placed in the center of a cold cubic enclosure, and is numerically simulated using the direct forcing immersed boundary (IB) method. Flow characteristics for both EHD and ETHD flows within this configuration are thoroughly analyzed, both quantitatively and qualitatively, across a representative range of operating parameters. Analyzing ETHD flows results in a more than threefold increase in heat flux from the hot embedded electrode compared to natural convection alone. This study highlights both the similarities and the differences in flow and heat transfer characteristics between the realistic $3D$ configuration and its $2D$ counterpart, paving the way for further application of the direct forcing IB method in the analysis of EHD and ETHD flows typical of realistic configurations.

1. Introduction

Electro-hydrodynamics (EHD) and electro-thermo-hydrodynamics (ETHD) are two branches of fluid mechanics, both governed by the interactions between electric fields and the fluid medium. In these phenomena, electric fields act on induced charges or charge distributions within the fluid, creating body forces that drive fluid motion. Additionally, in both cases, these electric fields can be modulated or influenced by external factors, such as temperature gradients in the case of ETHD, resulting in complex flow behaviors. Both EHD and ETHD have laid the foundation for numerous engineering advances. For example, EHD principles have been employed in the design of air ionizers [1], electrohydrodynamic thrusters [2], and commercial printer technologies [3]; ETHD flow analysis has been applied to improve solar energy systems [4] and to enhance the efficiency of thermal heat exchange in cooling [5], boiling and condensing [6], as well as drying and evaporating [7] processes, to name just a few. Most of the above applications use dielectric liquids as the medium between the two electrodes due to their high breakdown voltage, good heat transfer properties and chemical stability. For this reason, the current study also uses dielectric liquids for performance analysis. Both EHD and ETHD

* Corresponding author.
E-mail address: mukesh@post.bgu.ac.il (M. Kumar).

https://doi.org/10.1016/j.csite.2024.105438
Received 6 March 2024; Received in revised form 21 October 2024; Accepted 4 November 2024

Available online 22 November 2024

can only exist in the presence of free charge carriers, which can be generated by various mechanisms, including charge injection from the electrode and the induction of electric charges by electric field dissociation or by the variation of electrical conductivity. In dielectric liquids the injection mechanism is dominant in comparison with other free charge sources [8]. Hence, in this work we exclusively consider charge injection as a only source of uni-polar charges.

One of the most promising applications of ETHD phenomena is the enhancement of heat transfer from heated surfaces immersed within the fluid flow, which offers a distinct advantage over natural convection [9]. The key idea is to create sufficiently high electrical forces throughout the flow field to overcome the buoyancy force acting in the opposite direction to the temperature gradient, so that the unidirectional thermal plume is replaced by a series of electrically driven plumes distributed over the entire surface of a cooled electrode, immersed into a dielectric fluid. Experimental studies investigating the potential of ETHD for improving heat transfers from immersed surfaces are scarce, and limited to simple geometries. These include the enhancement of heat transfer rate between parallel plates [10], on an upward facing plate [11] and on the surface of a copper rod [12], as well as the enhancement of nucleate boiling on the surface of small injecting electrode [13].

In a number of research works, numerical analysis has been used to gain a better understanding of the potential of using ETHD to improve the heat transfer both in $2D$ and $3D$ geometries. Regarding $2D$ analysis in canonical geometries, worth mentioning are [14–20], which investigate the characteristics of ETHD flows in an enclosures and between parallel plates. Specifically, Yang et al. [14] investigated the potential of non-uniform electric fields in enhancement of heat transfer at low Rayleigh numbers. Wu and Traoré [15] extended this investigation to higher Rayleigh numbers with dielectric fluids. Wu et al. [16] further explored heat transfer enhancement in ETHD by introducing additional electric fields in Rayleigh–Bénard convection. Wang et al. [17] simulated ETHD with uniform and sinusoidal boundary conditions, finding non-uniform temperatures create complex flows. Selvakumar et al. [18] studied 2D ETHD convection, focusing on unipolar ion injection effects. Son and Park [19] demonstrated significant heat transfer enhancement using alternately arranged electrodes on vertical walls in a square cavity, while Liang et al. [20] investigated the complex interactions of electric fields with double-diffusive convection in a rectangular cavity, showing improved heat and mass transfer rates.

An evaluation of the effect of conjugate solid–liquid heat transfer on the heat transfer rate appears in [21], who found that the heat transfer rate decreases when the effect of thermal conduction within a solid wall of finite thickness is taken into account. Numerical simulations of more complex $2D$ configurations can be found in [22] focused on the role of carbon nanotubes and electric fields in enhancing heat transfer, while Li et al. [23] conducted parametric studies on oscillatory electro-thermo-convective flows, which investigate the ETHD flows inside concentric and eccentric circular annuli, respectively. Additionally, studies by [24–27] employed the lattice Boltzmann method to analyze ETHD flows between the walls of a square enclosure and various electrode configurations, including a circular electrode, elliptic electrode, and a pair of cylindrical electrodes. The study published in [27] was then extended in [28] to the analysis of non-Newtonian charge carriers, focussing on how the hysteresis loop depth depends on the power-law index of the fluid. In relation to $3D$ analysis, the major research effort has been in studying transition to unsteadiness in a dielectric liquid separating two parallel plates [29] and in enhancing the mixing of the flow species in an infinitely long multichannel [30]; these to the best of the authors' knowledge, are the only works addressing three-dimensional electro-driven flows.

The goal of the present study is twofold. Our first objective is to demonstrate the capabilities of the direct forcing immersed boundary (IB) method for addressing general $3D$ EHD and ETHD flows. The direct forcing IB approach is not a standalone methodology and should be implemented on top of a more basic solver for the governing equations, for example, standard finite volume method or lattice Boltzmann approach, see e.g. [31–34].

Remarkably, to date, the capabilities of the direct forcing IB approach in ETHD flows have not been fully exploited, apart from the study by [26], which used the IB-lattice Boltzmann method for analyzing ETHD flows in 2D configurations. The currently developed methodology, which constitutes an extension of our recently developed framework [35] to electro-driven flows, bridges the above gap. To do this, we couple the incompressible Navier–Stokes and energy equations with the Poisson–Nernst–Planck (PNP) and the electrostatic system of equations governing the transport of charged species and the spatial distribution of electric potential, respectively. The overall system of equations is solved in a segregated manner, while coupling between all fields is achieved using the SIMPLE algorithm and the internal PNP iterations. A pseudo-time technique is employed to facilitate the solution of the large Poisson system of equations for the electric potential.

Our second objective is to investigate both the EHD and the ETHD flows developing between the hot spherical electrode placed in the center of a cubic enclosure filled with dielectric liquid subject to the unipolar injection and voltage. Here our focus is on the investigation of the distribution of temperature, charge density and the vortex structures developing over the entire range of operating parameters, as well as on careful examination of the mechanism of transition to unsteadiness of both EHD and ETHD flows. The capabilities of the ETHD flow for increasing the rate of heat transfer from the surface of a hot spherical electrode are discussed, and the fundamental differences between the heat transfer mechanism typical of the currently investigated $3D$ configuration and its $2D$ counterpart are highlighted.

2. Governing equations

We consider the ETHD flow, which combines the phenomena observed in fluid mechanics, heat transfer, and electro-kinetics. The flow is governed by the system of continuity, momentum, energy, electro-static and charge density conservation equations that read:

$$\tilde{\nabla} \cdot \tilde{\boldsymbol{u}} = 0, \tag{1}$$

$$\frac{\partial(\rho_o\tilde{\boldsymbol{u}})}{\partial t} + \tilde{\nabla}\cdot(\rho_o\tilde{\boldsymbol{u}}\tilde{\boldsymbol{u}}) = -\tilde{\nabla}\tilde{p} + \rho_o\nu\tilde{\nabla}^2\tilde{\boldsymbol{u}} + \tilde{q}\tilde{\nabla}\tilde{\phi} + \tilde{\rho}\boldsymbol{g}, \tag{2}$$

$$\frac{\partial\tilde{\theta}}{\partial\tilde{t}} + \tilde{\nabla}\cdot(\tilde{\boldsymbol{u}}\tilde{\theta}) = \frac{\kappa}{\rho_o C_p}\tilde{\nabla}^2\tilde{\theta}, \tag{3}$$

$$\tilde{\nabla}^2\tilde{\phi} = -\frac{\tilde{q}}{\varepsilon}, \tag{4}$$

$$\frac{\partial\tilde{q}}{\partial\tilde{t}} + \tilde{\nabla}\cdot(\tilde{q}\tilde{\boldsymbol{u}} - K\tilde{q}\tilde{\nabla}\tilde{\phi} - D\tilde{\nabla}\tilde{q}) = 0, \tag{5}$$

where $\tilde{\boldsymbol{u}}$ denotes the velocity vector $[\tilde{u}, \tilde{v}, \tilde{w}]$, $\tilde{p}$ is the hydrodynamic pressure, $\tilde{\theta}$ refers to the temperature field, $\tilde{\phi}$ is the electric potential, and $\tilde{q}$ is the charge density field. The effects of gravity and electric fields are accounted for as the source terms in the momentum equation. K denotes the ionic mobility, $\tilde{\rho}$ is the fluid density, ν represents the kinematics viscosity, κ is the thermal conductivity, and ε is the electrical permittivity. $\boldsymbol{g}$ is the gravity vector, D refers to the molecular diffusion coefficient, and $\tilde{t}$ is the time. ρ_0, represents the density field corresponding to the reference temperature, θ_0, and β is the coefficient of thermal expansion. Note that we currently focus only on the impact of the Coulomb force since for incompressible flows the dielectric and the electrostriction forces can be included within the pressure term [36]. We non-dimensionalize the above governing equations using suitable reference scales, as given below:

$$\boldsymbol{x} = \frac{\tilde{\boldsymbol{x}}}{H}, \quad t = \tilde{t}\frac{\nu}{H^2}, \quad \boldsymbol{u} = \tilde{\boldsymbol{u}}\frac{H}{\nu}, \quad p = \tilde{p}\frac{H^2}{\rho_0\nu^2}, \phi = \frac{\tilde{\phi}}{\Delta\phi}, \quad q = \frac{\tilde{q}}{q_0}, \quad \rho = \frac{\tilde{\rho}}{\rho_0}, \quad \theta = \frac{\tilde{\theta}-\theta_0}{\Delta\theta}, \tag{6}$$

where $\boldsymbol{x}$ corresponds to the Cartesian coordinates vector, and H and q_0 refer to the characteristic length and the charge density scales, respectively. $\Delta\phi$ denotes the potential difference $\phi_0 - \phi_1$, and $\Delta\theta$ is the temperature difference $\theta_h - \theta_c$, where θ_c and θ_h are the cold and hot temperatures, respectively. We choose a velocity scale based on the kinematic viscosity, which is arguably the physically correct choice of a reference velocity for electro-thermally driven flows. Other choices of velocity scale are also possible, although they would result in a different form of the non-dimensional governing equations. We next formulate the non-dimensional governing equations as:

$$\nabla\cdot\boldsymbol{u} = 0, \tag{7}$$

$$\frac{\partial\boldsymbol{u}}{\partial t} + \nabla\cdot(\boldsymbol{u}\boldsymbol{u}) = -\nabla p + \nabla^2\boldsymbol{u} - \frac{T^2}{M^2}Cq\nabla\phi + \frac{Ra}{Pr}\theta\vec{e_z}, \tag{8}$$

$$\frac{\partial\theta}{\partial t} + \nabla\cdot(\boldsymbol{u}\theta) = \frac{1}{Pr}\nabla^2\theta, \tag{9}$$

$$\nabla^2\phi = -\boldsymbol{C}\cdot q, \tag{10}$$

$$\frac{\partial q}{\partial t} + \nabla\cdot(\boldsymbol{u}q) = \hat{D}\nabla^2 q + \nabla\cdot(q\frac{T}{M^2}\nabla\phi). \tag{11}$$

The non-dimensional groups appearing in the equations are the Prandtl number, Pr, the Rayleigh number, Ra, and the electric Rayleigh number, T defined as:

$$Ra = \frac{\vec{g}\beta\Delta\theta H^3}{\kappa\nu}, \quad Pr = \frac{\nu}{\alpha_0}, \quad T = \frac{\varepsilon\phi_0}{\rho\nu K}. \tag{12}$$

Additional non-dimensional coefficients appearing in equations are the injection strength number, C, the mobility number M, and the molecular diffusion coefficient, $\hat{D}$ defined as:

$$C = \frac{q_0 H^2}{\varepsilon\phi_0}, \quad M = \frac{1}{K}\sqrt{\frac{\varepsilon}{\rho}}, \quad \hat{D} = \frac{D}{\nu}. \tag{13}$$

3. Numerical methodology

This section provides a brief overview of the discretization of the governing equations and the numerical algorithm used in the current work for the solution of the governing equations. The spatial discretization employs a finite volume method on a staggered grid. The u, v, and w velocity component fields are staggered by a half grid cell in the horizontal, spanwise and vertical directions, respectively, with respect to the scalar fields. A SIMPLE method is used for the pressure-velocity coupling. All the linear terms are treated implicitly, while all the non-linear terms, including the convective flux, electric body force and electro-migration terms, are taken explicitly from the previous time step. We use the standard second order central difference scheme for discretizing all the diffusive, electric body force and electro-migration terms, while all the convective fluxes are discretized by utilizing the second order upwind scheme. A second order backward finite difference scheme is used for the time discretization.

The algorithm sequence for advancing by a single time step is summarized as follows:

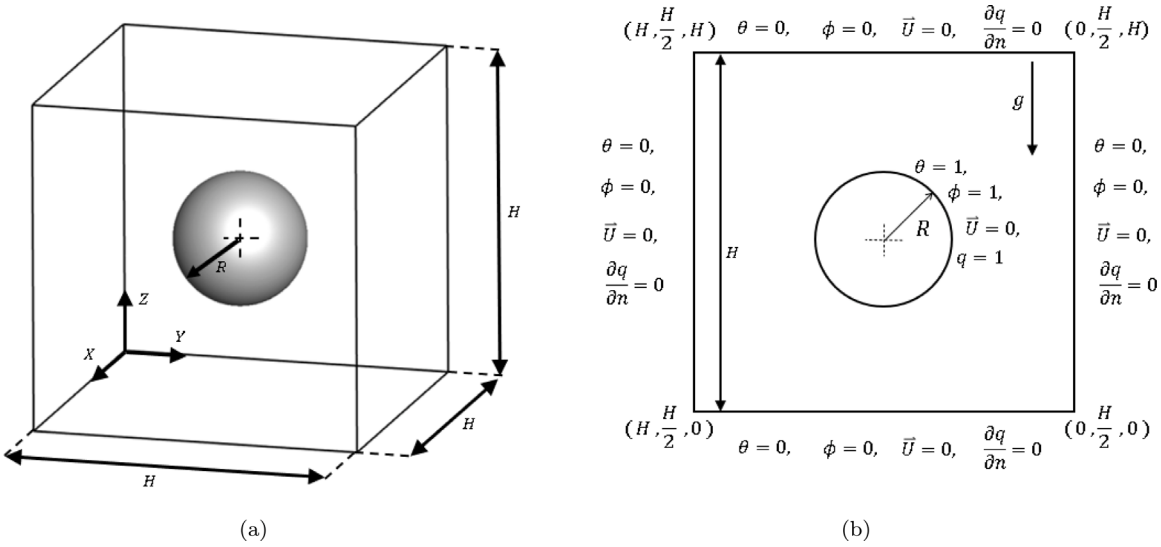

Fig. 1. (a) Schematic diagram of a cubic enclosure hosting a sphere placed in its center; (b) mid cross-section taken at $X = 0.5$ plane with all the boundary conditions.

1. Initialization of $\boldsymbol{u}$, p, ϕ, θ, and q fields
2. Solution of the Poisson–Nernst–Planck (PNP) equations
   (a) Solution of the electro-static equation formulated in terms of the electric potential $\nabla^2\phi = -C \cdot q^n$ (see Eq. (10))
   (b) Solution of the charge density transport equation $\frac{3q^{n+1}}{2\Delta t} - \hat{D}\nabla^2 q^{n+1} = -\nabla \cdot (\boldsymbol{u}q)^n + \nabla \cdot (q\frac{T}{M^2}\nabla\phi)^n + \frac{4q^n - q^{n-1}}{2\Delta t}$ (see Eq. (11))
   (c) Performing internal PNP iterations until the convergence of ϕ and q^{n+1} is achieved by:
      i. assigning q^{n+1} obtained upon completion of (b) to the RHS of (a)
      ii. assigning ϕ obtained upon completion of (a) to the $\nabla \cdot (q\frac{T}{M^2}\nabla\phi)^n$ term in the RHS of (b)
3. Solution of the energy equation $\frac{3\theta^{n+1}}{2\Delta t} - \frac{1}{Pr}\nabla^2\theta^{n+1} = -\nabla \cdot (\boldsymbol{u}\theta)^n + \frac{4\theta^n - \theta^{n-1}}{2\Delta t}$ (see Eq. (9))
4. Solution of the momentum and continuity equations by applying the SIMPLE method [37] for the pressure-velocity coupling:
   (a) $\frac{3\boldsymbol{u}^*}{2\Delta t} - \nabla^2\boldsymbol{u}^* = -\nabla p^n - \frac{T^2}{M^2}Cq\nabla\phi + \frac{Ra}{Pr}\theta^{n+1}\vec{e}_z - \nabla \cdot (\boldsymbol{u}\boldsymbol{u})^n + \frac{4\boldsymbol{u}^n - \boldsymbol{u}^{n-1}}{2\Delta t}$
   (b) $\nabla^2 p' = \frac{3}{2\Delta t}\nabla \cdot \boldsymbol{u}^*$
   (c) $p^{n+1} = p^n + p', \boldsymbol{u}^{n+1} = \boldsymbol{u}^* + \boldsymbol{u}'$
5. Proceed to step 2.

All the equations listed in steps 2–4 incorporate either the Helmholtz or the Stokes operators; this makes it possible to solve the whole system by utilizing the direct tensor product factorization (TPF) based solver [38] by employing it successively for resolving each field. Note also that the above formulation constitutes the most general framework, making it possible to address electro-thermo-convection phenomena subject to applying specific boundary conditions. In the following we detail the configuration addressed in the framework of the current study, as well as the IB method used to impose the relevant boundary conditions.

4. Physical model

An EHD flow within a cold cubic enclosure of unity side length hosting a hot sphere of radius $R = 0.2$ placed at the cavity center is considered (see Fig. 1a). This configuration enables the analysis of complex interactions between electric and buoyancy fields, typical of a spherically shaped injecting electrode placed within a cubic enclosure filled with a dielectric liquid such as mineral oil. The enclosure walls constitute completely open electrodes which are held at constant cold temperature $\theta = 0$ and constant electric potential $\phi = 0$. The surface of the sphere is considered to be an autonomous injecting electrode held at constant hot temperature $\theta = 1$ and constant electric potential $\phi = 1$. Non-slip boundary conditions are applied for all the velocity components on all the enclosure and the sphere surfaces. A full set of the applied boundary conditions is given in Fig. 1b.

5. Immersed boundary formulation

5.1. Governing equations

The boundary conditions on the surface of the sphere are enforced by utilizing the direct forcing IB method [35,39]. Following the formalism of the direct forcing IB method, the problem is discretized on two independent grids, namely, the Eulerian and the Lagrangian grids. The Eulerian grid constitutes a structured grid on which the governing equations are solved. The Lagrangian grid is determined by a series of discrete points uniformly distributed over the sphere surface. The impact of the body surface on the surroundings is reflected by applying the dynamic conditions which appear in the governing equations as additional sources. The sources placed at each Lagrangian point play the role of Lagrange multipliers and their values are unknown a priori. To achieve the closure the kinematic constraints of no-slip and the prescribed values of temperature, electric potential and concentration on the sphere surface are added to the overall system. The extended set of equations is given by:

$$\nabla \cdot \boldsymbol{u} = 0, \tag{14}$$

$$\frac{\partial \boldsymbol{u}}{\partial t} + \nabla \cdot (\boldsymbol{u}\boldsymbol{u}) = -\nabla p + \nabla^2 \boldsymbol{u} - \frac{T^2}{M^2} C q \nabla \phi + \frac{Ra}{Pr} \theta \vec{e}_z + \boldsymbol{R}[\boldsymbol{F_u}], \tag{15a}$$

$$\boldsymbol{I}(\boldsymbol{u}) = \boldsymbol{U}^{\Gamma}, \tag{15b}$$

$$\frac{\partial \theta}{\partial t} + \nabla \cdot (\boldsymbol{u}\theta) = \frac{1}{Pr} \nabla^2 \theta + \boldsymbol{R}[F_\theta], \tag{16a}$$

$$\boldsymbol{I}(\theta) = \boldsymbol{\Theta}^{\Gamma}, \tag{16b}$$

$$\nabla^2 \phi = -C \cdot q + \boldsymbol{R}[F_\phi], \tag{17a}$$

$$\boldsymbol{I}(\phi) = \boldsymbol{\Phi}^{\Gamma}, \tag{17b}$$

$$\frac{\partial q}{\partial t} + \hat{D} \nabla^2 q = \nabla \cdot (q \frac{T}{M^2} \nabla \phi - q\boldsymbol{u}) + \boldsymbol{R}[F_q], \tag{18a}$$

$$\boldsymbol{I}(q) = \boldsymbol{Q}^{\Gamma}, \tag{18b}$$

where $\boldsymbol{U}^{\Gamma}$ represents the non-slip boundary condition, $\boldsymbol{\Theta}^{\Gamma}$, $\boldsymbol{\Phi}^{\Gamma}$, and $\boldsymbol{Q}^{\Gamma}$ correspond to the temperature, electric potential and charge density values, respectively, preset on the surface of immersed body. $\boldsymbol{I}$ and $\boldsymbol{R}$ correspond to the interpolation and regularization operators, respectively, utilized for conveying the information between the Lagrangian and Eulerian grids:

$$f_i(\boldsymbol{x}) = \boldsymbol{R}[F_k(\boldsymbol{X})] = \int_{V_s} F_k(\boldsymbol{X}) \cdot \delta(\boldsymbol{x} - \boldsymbol{X}) dV_S, \tag{19a}$$

$$\Psi_k(\boldsymbol{X}) = \boldsymbol{I}[\psi_i(\boldsymbol{X})] = \int_{\Omega} \psi_i(x) \cdot \delta(\boldsymbol{X} - \boldsymbol{x}) dV_\Omega, \tag{19b}$$

where F_k corresponds to the scalar volumetric quantity from the list of $\{F_{u_x}, F_{u_y}, F_{u_z}, F_\theta, F_\phi, F_q\}$ taken in the kth Lagrangian point of the surface of the immersed body, and ψ_i corresponds to the ith Eulerian variable from the list of $\{u_x, u_y, u_z, \theta, \phi, q\}$. V_S and V_Ω correspond to the finite volumes confining Lagrangian and Eulerian variables, respectively. These volumes should be approximately the same to provide well conditioning of the governing operators. Introducing next the local coordinates of kth Lagrangian point $(\epsilon_k, \eta_k, \zeta_k)$ Eqs. (19) can be reformulated in a discrete form as:

$$f_i(\boldsymbol{x}) = \Delta x^3 \sum_k (F_k(\boldsymbol{X})) \delta(\epsilon_k - x_i) \delta(\eta_k - y_i) \delta(\zeta_k - z_i), \tag{20}$$

$$\Psi_k(\boldsymbol{X}) = \Delta x^3 \sum_i (\psi_i(\boldsymbol{X})) \delta(x_i - \epsilon_k) \delta(y_i - \eta_k) \delta(z_i - \zeta_k). \tag{21}$$

Here $\delta(r)$ is the one dimensional discrete Dirac delta function introduced in [40]:

$$\delta(r) = \begin{cases} \frac{1}{6\Delta r}\left[5 - 3\frac{|r|}{\Delta r} - \sqrt{-3(1 - \frac{|r|}{\Delta r})^2 + 1}\right] & \frac{1}{2}\Delta r \le |r| \le \frac{3}{2}\Delta r. \\ \frac{1}{3\Delta r}\left[1 + \sqrt{-3(\frac{|r|}{\Delta r})^2 + 1}\right] & |r| \le 0.5\Delta r, \\ 0 & \text{otherwise}, \end{cases} \tag{22}$$

where Δr is the cell width in the r direction. The above delta function has a compact support of only three grid cells in each direction. It has been specifically designed for performing calculations on staggered grids and has gained popularity over recent years [41–43]. To achieve the best accuracy of the results and to avoid ill-conditioning of the operators governing Eqs. (15)–(18), the spacing between neighbor Lagrangian points on the surface of the immersed body should be close to the grid size of the corresponding Eulerian grid. To map the spherical surface we used the non-iterative method of Leopardi [44]. Note that each set of the governing equations with the corresponding dynamic and kinematic constrains corresponding to the continuity and momentum equations (Eqs. ((14)–(15)a–b)), energy equation (Eqs. ((16)a-b)), electrostatic potential equation (Eqs. ((17)a–b)), and space charge density equation (Eqs. ((18)a–b)) and the corresponding boundary conditions constitute a closed set of equations solved by the methodology described in the next section.

5.2. Solution methodology

The governing Eqs. (14)–(18) were discretized and solved in the same sequence as that described in Section 3. All the additional unknowns were treated implicitly with the fields governed by the corresponding transport equations; these additional unknowns, in fact, appeared as a result of applying the IB method and due to the regularized volumetric sources. The strategy, which is similar to that applied in our previous study [35], is as follows. Each pair of Eqs. ((15), (16), (18)) can be compactly reformulated in a block-matrix form as:

$$\begin{bmatrix} \boldsymbol{H}_{\boldsymbol{u}^*,\theta,q} & \boldsymbol{R} \\ \boldsymbol{I} & 0 \end{bmatrix} \begin{bmatrix} \boldsymbol{u}^*, \theta, q \\ \boldsymbol{F}_{\boldsymbol{u}^*}, F_\theta, F_q \end{bmatrix} = \begin{bmatrix} RHS^{n,n-1}_{\boldsymbol{u}^*,\theta,q} \\ \boldsymbol{U}^\Gamma, \Theta^\Gamma, Q^\Gamma \end{bmatrix}, \tag{23}$$

where $\boldsymbol{H}$ is the Helmholtz operator acting on $\boldsymbol{u}^*$, θ, and q fields. Note that the non-solenoidal field $\boldsymbol{u}^*$, obtained in this way is then projected to the divergence free subspace by a standard SIMPLE method, as detailed in the previous section. The system of Eqs. (17) governing the electrostatic potential is stationary, and therefore, after replacing the Helmholtz operator $\boldsymbol{H}$ by the Laplacian operator $\boldsymbol{L}$ it can also be reformulated in the block-matrix form as:

$$\begin{bmatrix} \boldsymbol{L} & \boldsymbol{R} \\ \boldsymbol{I} & 0 \end{bmatrix} \begin{bmatrix} \phi \\ F_\phi \end{bmatrix} = \begin{bmatrix} RHS_\phi \\ \boldsymbol{\Phi}^\Gamma \end{bmatrix}. \tag{24}$$

We next apply the Schur complement approach to analytically decompose system (23) into:

$$[\boldsymbol{F}_{\boldsymbol{u}^*}, F_\theta, F_q] = [\boldsymbol{I}\boldsymbol{H}^{-1}_{\boldsymbol{u}^*,\theta,q}\boldsymbol{R}]^{-1}[\boldsymbol{I}\boldsymbol{H}^{-1}_{\boldsymbol{u}^*,\theta,q}RHS^{n,n-1}_{\boldsymbol{u}^*,\theta,q} - \boldsymbol{U}^\Gamma, \Theta^\Gamma, Q^\Gamma], \tag{25a}$$

$$[\boldsymbol{u}^*, \theta, q] = \boldsymbol{H}^{-1}_{\boldsymbol{u}^*,\theta,q}[RHS^{n,n-1}_{\boldsymbol{u}^*,\theta,q} - \boldsymbol{R}[\boldsymbol{F}_{\boldsymbol{u}^*}, F_\theta, F_q]], \tag{25b}$$

and system (24) into:

$$F_\phi = [\boldsymbol{I}\boldsymbol{L}^{-1}\boldsymbol{R}]^{-1}[\boldsymbol{I}\boldsymbol{L}^{-1}RHS^{n,n-1}_\phi - \boldsymbol{\Phi}^\Gamma], \tag{26a}$$

$$\phi = \boldsymbol{L}^{-1}[RHS^{n,n-1}_\phi - \boldsymbol{R}F_\phi]. \tag{26b}$$

In the next step we incorporate the TPF based solver [38] for the purpose of performing matrix–vector products of the inverse Helmholtz and Laplacian operators (see Ref. [35] for more details) and successively solve Eqs. (25)–(26) to obtain all the unknown fields. Lastly, with regard to the solution of Eq. (26), for realistically large grid resolutions (more than 200 grid cells in each direction) we obtain an extremely ill-conditioned matrix $[\boldsymbol{I}\boldsymbol{L}^{-1}\boldsymbol{R}]$, which leads to prohibitively high memory consumption or to severe convergence problems when further attempting to calculate F_ϕ by either direct (LU decomposition) or iterative (BicgStab) methods. It is remarkable that this problem does not show up when performing the solution of Eqs. (25); this can be explained by its time dependance, such that a sufficiently small time step increases the main diagonal of the system and improves significantly its condition number. For this reason a pseudo time approach is applied for the solution of the system of Eqs. (24). The key idea is to introduce an additional time dependant parameter ϕ as follows:

$$\frac{\phi^{k+1}}{\Delta\tau} + \boldsymbol{L}(\phi^{k+1}) - \boldsymbol{R}(F_\phi) = \frac{\phi^k}{\Delta\tau} - C \cdot q^n, \tag{27a}$$

$$\boldsymbol{I}(\phi^{k+1}) = \boldsymbol{\Phi}^\Gamma(X). \tag{27b}$$

A series of iterations is then performed to reduce the value of the difference between ϕ^{k+1} and ϕ^k at each subsequent iteration. The iterations, typically ranging from 6 to 8 in number, are repeated until the steady state solution of the original problem is obtained with the required degree of accuracy.

6. Verification study

6.1. EHD flow: circular cylinder placed in the center of square cavity

We examine two-dimensional EHD flow regime developing around a circular cylinder placed in a square enclosure. The computational domain is discretized by uniform Cartesian 300 × 300 grid. The numerical simulations are performed for $M = 10$, $D = 10^{-4}$, $C = 10$ values, and three values of electric Rayleigh numbers equal to $T = 100$, $T = 300$, and $T = 600$. The obtained results are presented in Fig. 2(a, b, e, f, i, j) in terms of the of charge density and streamline distributions.

It can be seen that the obtained charge density and flow field characteristics exhibit symmetry with respect to both the horizontal and vertical centerlines, as well as the main diagonals of the domain. Although the flow field retains a similar structure of four pairs of convective cells across all values of T, the charge density distribution shows notable differences. At $T = 100$, the viscous force dampens the convection induced by the Coulomb force, resulting in weak convection. In this case, ions are primarily transported by the electric field through the drift mechanism, leading to high values of ion concentration in the cylinder vicinity and a smooth space charge distribution across the main region. For $T = 300$, the Coulomb force strengthens, inducing a more intense radial motion with four pairs of counter-rotating cells. The present contours of charge density and flow field (Fig. 2) show a qualitatively good agreement with the corresponding results reported in [24]. The slight difference between the currently obtained and the reported contours of charge density and stream lines distributions can be attributed to the fact that Luo et al. [24] did not provide the color

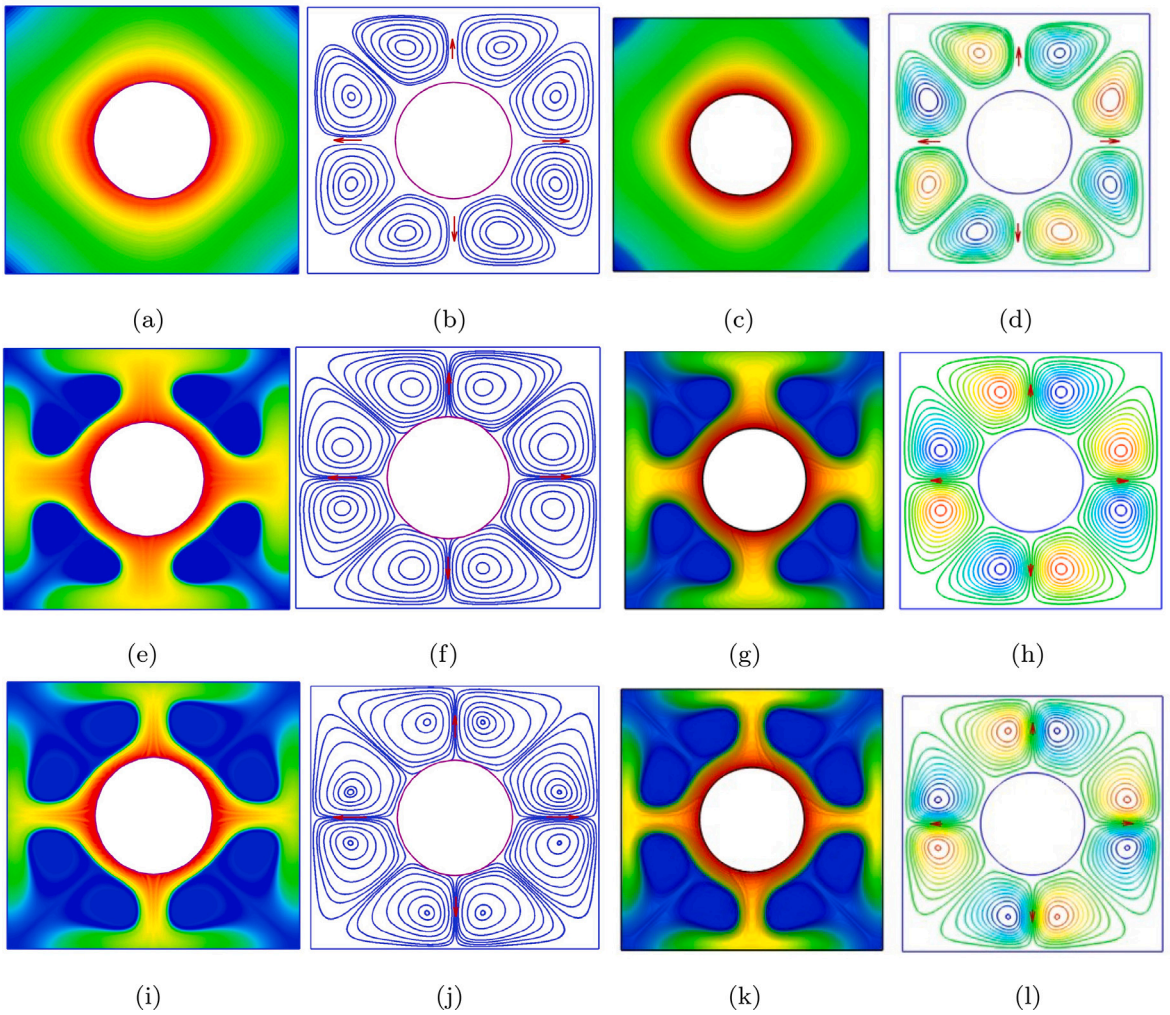

Fig. 2. A comparison between the currently obtained charge density and streamline distributions (two left columns) with the corresponding data reported in [24] (two right columns). The distributions obtained for $Ra = 10^5$ at (a, b) $T = 100$; (e, f) $T = 300$; (i, j) $T = 600$ are compared with the corresponding data reported in [24].
Source: Reproduced with permission from K. Luo et al. heat transfer enhancement in electro thermo-convection in a square enclosure with an inner circular cylinder, Int. J. Heat Mass Transfer 113, 1070–1085 (2017).

bar values in their manuscript. At the same time, a quantitative comparison of the $\frac{V_{max}}{Re_E}$ in a computational domain, as presented in Table 1, agrees well with the results reported in Luo et al. [24] for all the electric Rayleigh numbers, successfully verifying the currently developed approach.

6.2. ETHD flow: circular cylinder placed in the center of square cavity

We consider the case of electro-thermo-convection in the same two-dimensional configuration discussed in the previous section. In this study, we investigate the interplay between Coulomb and gravitational forces, ranging from weak to strong Coulomb force regimes. Although simulations were conducted for several values of T, we focus on only two test cases at $T = 150$ and $T = 300$ for the sake of concision. Additionally, since the primary goal is to verify the algorithm, we use a relatively fine 300×300 Cartesian mesh and a constant $\Delta t = 10^{-7}$ for all the simulations. Numerical simulations are conducted with $Pr = 10$, $M = 10$, $\hat{D} = 2 \times 10^{-4}$, $Ra = 10^5$, and an injection strength number $C = 10$. The distributions of charge density, temperature, and stream function for $T = 100$ and $T = 300$ are shown in Fig. 3.

At $T = 150$ the flow structure in Fig. 3(a) reveals two large convection cells, which is consistent with the findings in existing literature [24]. We also observe that the smooth charge distribution (Fig. 3(a)) does not generate significant radial electro-convection, in agreement with the findings of [24] at the same value of T. As the Coulomb force becomes sufficiently strong at

Table 1
The ratio of the maximum fluid velocity to the electric Reynolds number $\frac{V_{max}}{Re_E}$ as a function of electric Rayleigh number, T, where $Re_E = T/M^2$.

T	Present	Ref. [24]
100	0.224	0.215
200	1.964	2.062
300	7.269	7.191
400	10.421	10.338
600	15.331	15.071

$T = 300$, it induces radial convection, resulting in four pairs of counter-rotating convective cells, as shown in Fig. 3(c). Additionally, the charge distribution exhibits four distinct void regions in the domain. It is observed that heat is transported through injection-induced radial convection, which accounts for the similar plume structures observed in both the temperature and charge density distributions, in agreement with those reported by Luo et al. [24]. At $T = 300$, the charge distribution clearly exhibits symmetry breaking with respect to both diagonals. Furthermore, the temperature distribution preserves its symmetries similarly to results provided by [24]. The slight differences observed in the contours of the charge density and temperature fields can again be attributed to the fact that Luo et al. [24] did not provide the color bar in their manuscript. All the above observations further successfully verify the currently developed methodology for simulating ETHD flows in enclosures.

6.3. Concentric ejecting spherical electrodes in an ohmic regime

As has already been stated, the current study is a first attempt to address fully $3D$ thermo-electro-convective flow developing around an ejecting spherical electrode placed within a cubic enclosure filled with a dielectric liquid. Hence, there is no available literature that can be straightforwardly used for verification of the currently developed methodology. Therefore, in order to verify the developed solver we focus on the calculation of the charge density and potential distributions developing between two concentric ejecting spherical electrodes in an ohmic regime characterized by a low enough value of the electric Rayleigh number so that electro-convection is negligible. In this case we only solve the PNP Eqs. (17)–(18) by assuming zero velocity field. Following the formalism of the IB method, the spherical electrodes are placed in the center of a cube of length 1, as shown in Fig. 4. The analysis is performed for the whole $3D$ domain, although the domain of interest is restricted to the space confined by the two concentric electrodes. The values of the inner, R_i, and the outer, R_o, radiuses of the spherical electrodes are equal to 0.1 and 0.2, respectively:

$$R = r_i : \phi = 1, q = 2, \boldsymbol{u} = 0, \tag{28a}$$

$$R = r_o : \phi = 0, q = 1, \boldsymbol{u} = 0. \tag{28b}$$

The computational domain is discretized by using a uniform mesh, and the computations are carried out at $M = 49$ and $\hat{D} = 5{\times}10^{-4}$, a constant value of injection field $C = 10$, and three different values of electric Rayleigh number $T = 10, 25$ and 50. The properties chosen correspond to silicone oil, used as a working liquid in many experimental studies [45,46]. The constant injection field ensures strong injection and may be seen as a good approximation of the so-named Space-Charge-Limited (SCL) injection, which can be experimentally achieved by covering the electrode with a membrane [47]. The chosen range of the electric Rayleigh number, T, values ensures the existence of underlimiting charge transport for the given configuration.

For the above set of operation conditions, the current configuration is characterized by $1D$ variation (in the radial direction only) of the charge density field. Therefore the performed verification procedure focuses on comparing the charge density distribution obtained by the developed fully $3D$ solver incorporating the IB method and addressing Eqs. (14)–(18) for the iso-thermal flow with the corresponding results independently obtained by us by utilizing the specifically written Matlab script. In this case we neglect all the flow velocities and solve $1D$ PNP equations in spherical coordinates to obtain the distribution of potential and charge density fields between the sphere surfaces:

$$\frac{\partial}{\partial r}(r^2 \frac{\partial \phi}{\partial r}) = -r^2 C q, \tag{29a}$$

$$\frac{\partial}{\partial r}(r^2 \frac{\partial q}{\partial r}) = r^2 \frac{T}{M^2}\left[C q^2 - \frac{\partial \phi}{\partial r}\frac{\partial q}{\partial r}\right]. \tag{29b}$$

Boundary conditions for the electric potential and the charge density fields are chosen to be the same as for the fully $3D$ configuration (see Eqs. (28a) and (28b)). Since the system of Eqs. (29) is not linear, internal iterations are introduced to solve it numerically. The system is solved in a segregated manner by first solving for the Poisson equation ((29)(a)) for the electric potential field by taking the charge density field from the previous iteration. The calculated potential field is next plugged into the transport equation ((29)(b)) in order to obtain the concentration field. The process is reiterated until convergence of both fields is achieved. The discretization is carried with the second order finite difference method. Under-relaxation of both fields is employed to provide a robust convergence of the iterations.

The contours of charge density distribution in a cross-section between the spheres, obtained by numerical solution of the fully $3D$ problem, are shown in Fig. 5 for the value of $T = 50$. As expected, the obtained distribution is $1D$ and varies only in a radial direction. We certify that the maximal value of the flow velocity magnitude is below 10^{-4}, which successfully verifies the assumption

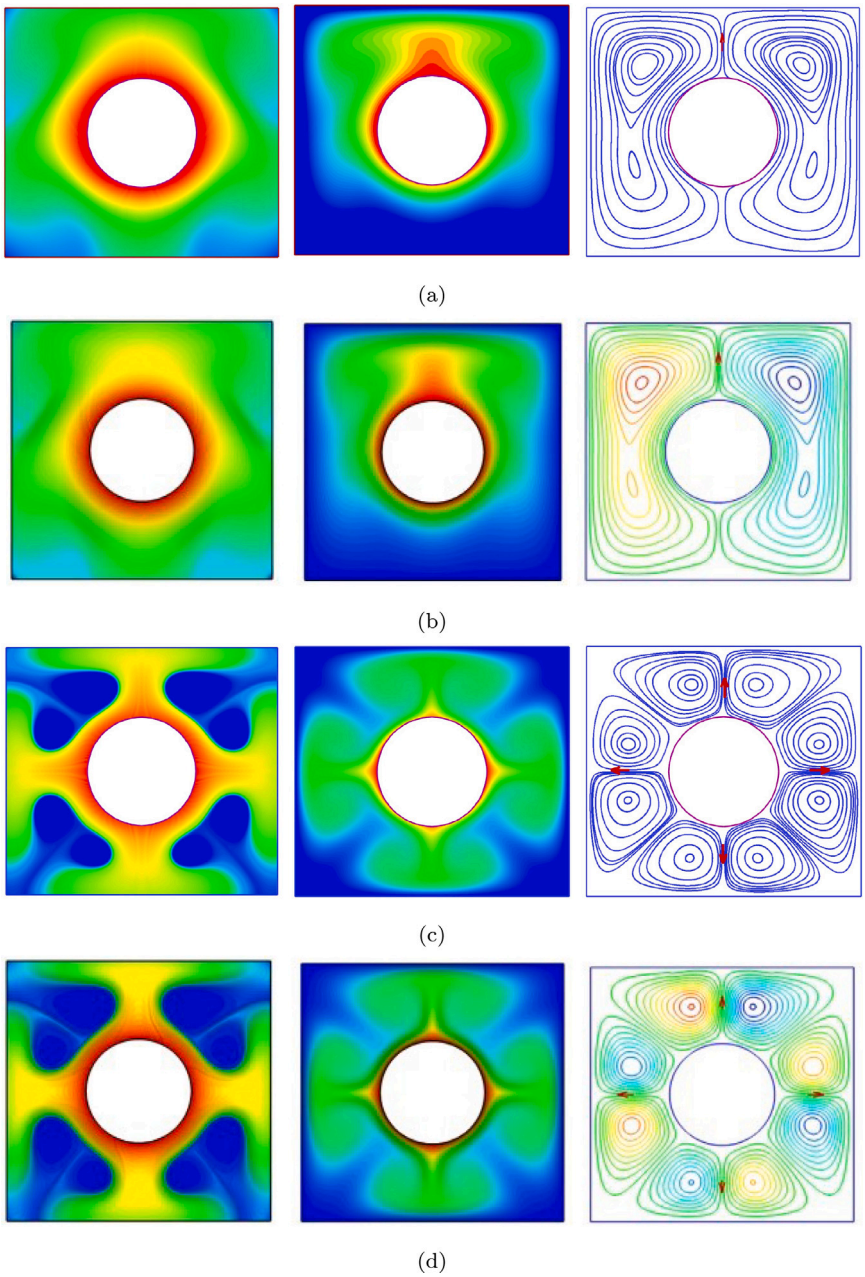

Fig. 3. A comparison between the currently obtained charge density (left), temperature(mid) and streamline (right) distributions (the first and the third rows) with the corresponding data reported in [24] (the second and the fourth rows). The results are obtained for the values of $Pr = 10$, $M = 10$, $\hat{D} = 2 \times 10^{-4}$, $Ra = 10^5$, and $C = 10$. The figures (a, b) correspond to the value of $T = 150$; the figures (c, d) correspond to the value of $T = 300$.
Source: Reproduced with permission from K. Luo et al. heat transfer enhancement in electro thermo-convection in a square enclosure with an inner circular cylinder, Int. J. Heat Mass Transfer 113, 1070–1085 (2017).

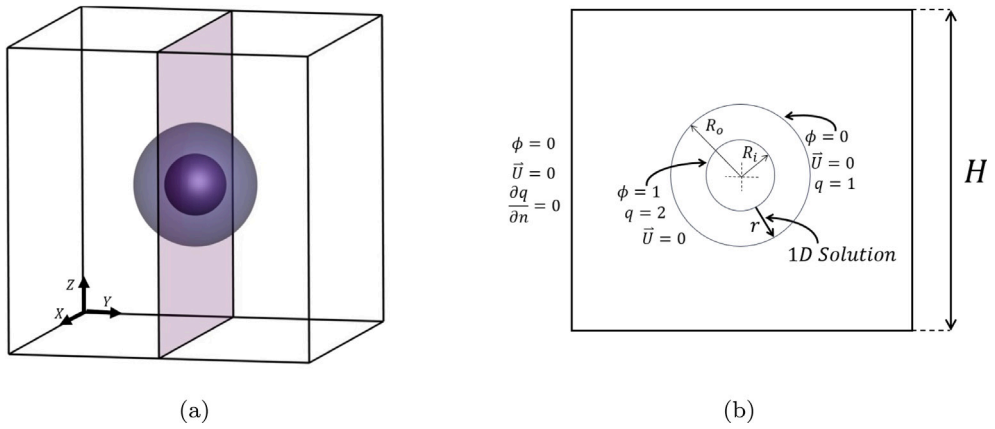

Fig. 4. A schematic of two concentric spheres placed within a cubic enclosure: (a) a fully $3D$ domain addressed by the developed IB solver; (b) a mid cross-section demonstrating the radial direction along which the problem is simulated by a specifically written Matlab script.

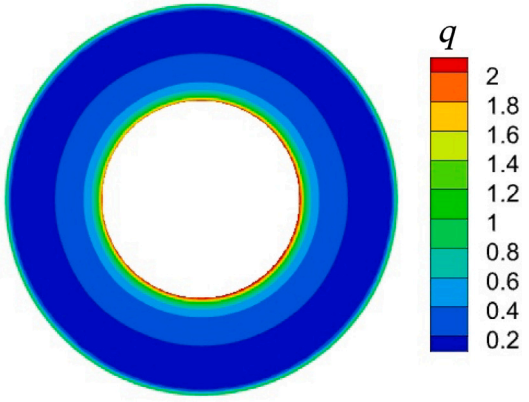

Fig. 5. Contours of charge density distribution between two concentric spheres.

of the negligible impact of electro-convection in the overall charge space transport for the given configuration. A comparison of the charge density distribution obtained by the $3D$ code with the corresponding fields obtained by the solution of axisymmetric PNP equations for different T values is shown in Fig. 6. It can be seen that there is good agreement between both results, while for the given configuration a grid independance between the $3D$ results is achieved for 300^3 grids. Hence, all the simulations presented in the framework of the current study were performed on 300^3 grids.

7. Results and discussion

7.1. Electro-convection flows

Both steady and unsteady isothermal electro-convection regimes are investigated for the configuration consisting of charged ejecting sphere placed in the center of a cubic enclosure (see Fig. 1 for details regarding the boundary conditions). All the computations are carried out at $Pr = 116.6$, $M = 49$ and $\hat{D} = 5 \times 10^{-4}$. Following the work of [47], the value of the injection strength is chosen to be to equal $C = 10$. The time steps lie in the range of $10^{-6} \leq \Delta t \leq 10^{-4}$ and depend on the value of the electric Rayleigh number T. The vortical structures of electro-convection are visualized by utilizing the λ_2 criterion based on the second largest eigenvalue λ_2 of the velocity gradient tensor, as discussed in [48]. Flow regions with negative values of λ_2 are characterized by the presence of vortices. A value of $\lambda_2 = -10$ is chosen for the visualization of convection cells. The convergence criterion for the steady state simulations performed in the current study is the value of 10^{-6} of the L_2 norm calculated for the difference between two consecutive time steps for all the flow fields. Unsteady simulations are continued until the maximum number of time steps is reached.

Seven distinct test cases are chosen to simulate electro-convection problems over a range of electric Rayleigh numbers. The steady state solutions is observed for the range of electric Rayleigh number $T \in [100 \div 800]$, while the values of T lying in the range of $T \in [800 \div 900]$ characterize the non-stationary flow regimes. The steady state flows is investigated in terms of the distribution of

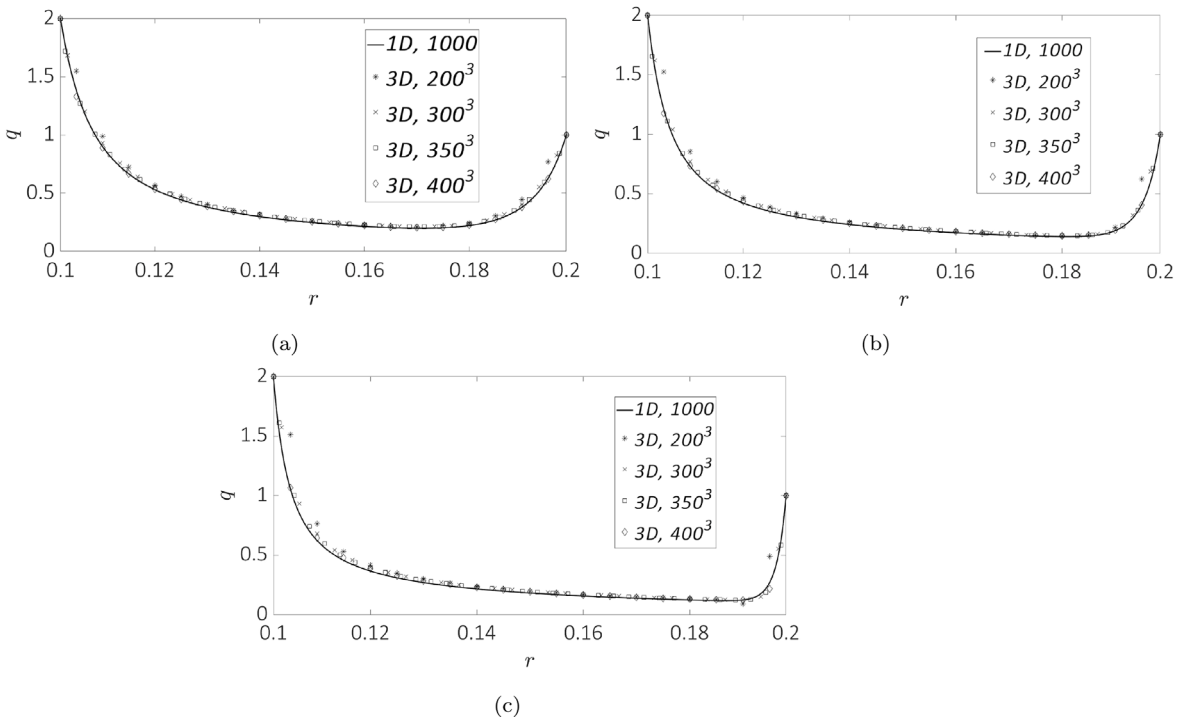

Fig. 6. Comparison between the charge density distribution along the radial direction with analytical solution at : (a) $T = 10$; (b) $T = 25$; (c) $T = 50$.

the charge density and path lines, projected on the cross-sectional and the main diagonal mid-planes, as well as by the iso-surfaces of the λ_2 criterion. The charge density distributions shown in Fig. 7(a–c) are characterized by the mid cross-section symmetry, which indicates that in the steady state regime there is no preferred direction in the ionic transport driven by the drift mechanism of the electric field. It should be noted that for small values of the electric Rayleigh number, $100 \leq T \leq 300$, viscous force dominates the Coulomb force governing electro-convection phenomena. As a result, the values of the velocity magnitude are low and convective cells cannot be clearly recognized for this range of T. The steady state flow obtained for $T = 700$ preserves mid cross-sectional symmetry and exhibits four pairs of counter-rotating vortices, as demonstrated in Fig. 7(d). It is characterized by four central regions where close-to-zero values of q are observed as a result of the local balance between the viscous and the electric forces typical of these regions, see e.g. [49,50]. We also remark that Coulomb-driven flows have a characteristic feature of a charge void regime when the Coulomb and viscous forces have a same order of magnitude. The qualitative trend of the charge void phenomenon is also observed in the literature for simulating $2D$ symmetrically-placed electrodes in the domain.

We next investigate the regimes typical of higher electric Rayleigh numbers $T \geq 700$ for which the symmetry breaking phenomenon of the electro-convective flow can be clearly recognized. Fig. 7(e) reveals the existence of thinner charge plumes, which is a consequence of increased electric field acting throughout the domain. It is worth noting that for high T values the ion transport in the domain is primarily governed by the flow convection mechanism since the drift velocity of ions is smaller than the flow velocity. This observation is clearly evident in Fig. 8 demonstrating the relationship between the maximum fluid velocity, V_{max}, and the electric Rayleigh number, T. Hence, almost all ions tend to adhere to the regions characterized by the highest flow velocity values. Fig. 8 reveals two regions distinguishing between the charge density transport regimes with respect to the value of T. The first region observed between $200 < T < 300$ corresponds to a charge void regime, while the second region, typical of the range of $800 < T < 900$, corresponds to an unsteady regime of the electro-convective flow. As can be clearly recognized from Fig. 8 the maximum velocity value is not zero for the entire range of T values — it is weak for $200 < T < 300$, gradually increasing with increasing T values. It is noteworthy that the behavior is different to that typical of configurations hosting symmetrically placed electrodes, which exhibit a sharp transition between entirely static and dynamic flow regimes.

7.2. Electro-thermo-convection flows

We next focus on an investigation of electro-thermo-convection flow for which the surface of a sphere placed in the center of a cold cubic enclosure is kept at hot constant temperature $\theta_h = 1$ while all the walls of the cubic enclosure are held at cold constant temperature $\theta_c = 0$. The analysis requires solving the energy equation in addition to the Poisson–Nernst–Planck system addressed in the previous section. The computational domain, boundary conditions and operating parameters are the same as in the previous section. The electro-thermo-convection is simulated for a Rayleigh number equal to $Ra = 10^5$. A series of numerical simulations

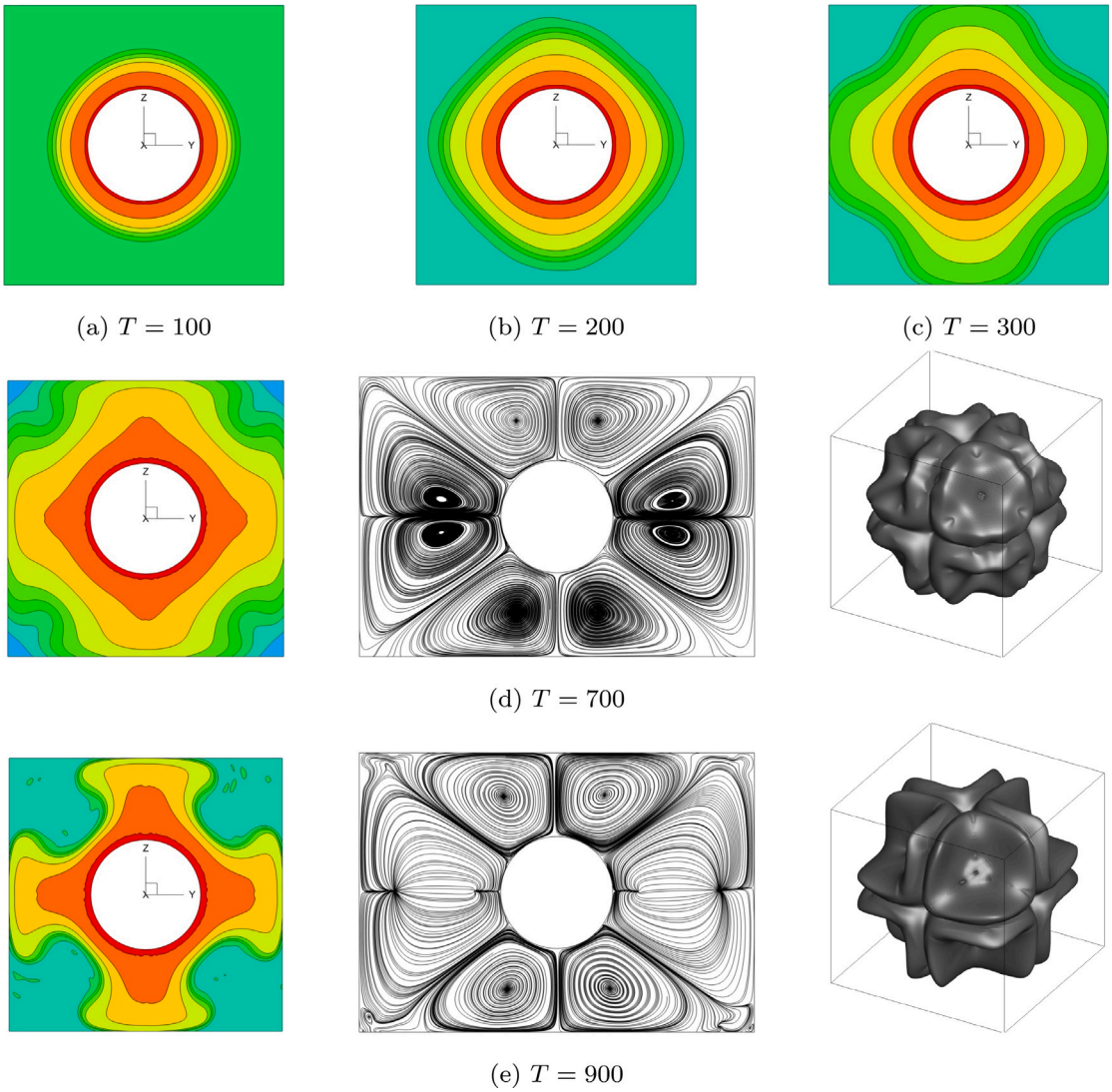

Fig. 7. (a–c) Distributions of charge density in a mid cross-section obtained for pseudo conduction regime. (d–e) Distribution of charge density in a mid cross-section (left); projection of path lines distribution onto main diagonal section (middle); iso-surfaces of $\lambda_2 = -10$ (right) obtained for electro-convection regime. The color palette consists of 10 evenly distributed contours with red color corresponding to $q = 1$ and blue color corresponding to $q = 0$ values.

are performed for a wide range of electric Rayleigh numbers $0 \leq T \leq 1300$. The obtained results reveal that the above range can be split into two sub-ranges: the first region $0 \leq T \leq 600$ characterizes the steady state (see Fig. 9), and the second region (see Fig. 10) characterizes the unsteady flow regimes, so that the transition between the steady and transient flow regimes sets in at $600 < T < 700$. It can be seen that the distributions of electric charge density and temperature fields of the steady state flow preserve mid plane cross-sectional symmetry with respect to both the $Z - Y$ and the $Z - X$ mid planes, and also with respect to the main diagonal plane (see Fig. 9). At higher values of the electric Rayleigh number, T, the symmetry breaking phenomenon can be clearly recognized both in the electric charge density and temperature distributions (see Fig. 10). It is also notable that up to $0 \leq T \leq 500$ the buoyancy force still dominates over the electro driven forces, so that only a single thermal plume exists with a clearly recognized direction from the surface of the hot sphere to the top lid of the cubic enclosure. The bottom part of the enclosure remains cold and practically no mixing is observed there between the hot and the cold fluids in this region. Further increase of the T value results in an increasing impact of the EDL forces, which for $T = 600$ leads to penetration of the warm fluid into the bottom part of the cubic enclosure. This phenomenon is exhibited by the formation of a secondary thermal plume in the opposite direction to the gravity force (i.e. from the cylinder surface towards the bottom of the cubic enclosure), as demonstrated in Fig. 9(g). Apparently, the penetration of the hot fluid into the bottom part of the enclosure that persists for the values of $600 < T$ constitutes the primary source of instability leading to the symmetry breaking phenomenon and to the transition to unsteadiness. In order to gain more insight into the flow characteristics of the considered electro-thermo-convection flow we next focus on its

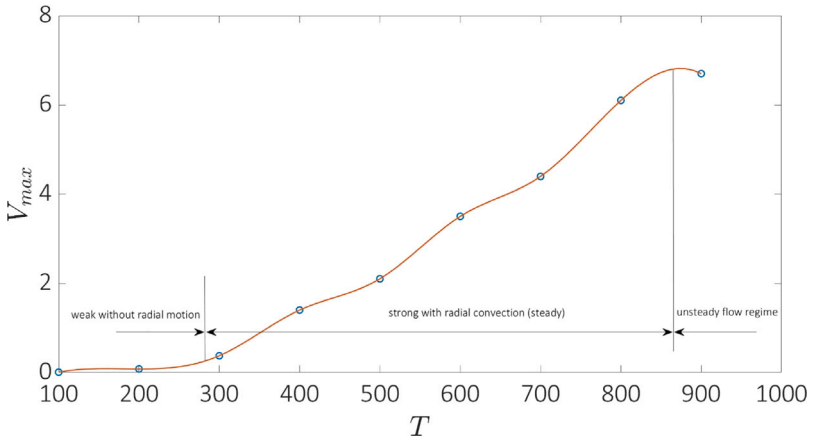

Fig. 8. Dependance of the maximal velocity value, V_{max}, on the electric Rayleigh number value, T, for pure electro-convection.

vortical structure for the entire range of $0 \leq T \leq 1300$ values. The vortical structure of electro-thermo-convection exhibits a variety of different scenarios with respect to different values of the electric Rayleigh number, as depicted in Fig. 11 and Fig. 12 for the steady and the transient flows, respectively. As has already been mentioned, for close-to-zero values of T the effects of electric field forces on the fluid are negligible, leading to a pure thermal convection regime (see Figs. 11(a)–(b)) as is also supported by looking at the corresponding vortical structures exhibiting mushroom-shaped vortical patterns typical of natural convection flows. As the electric Rayleigh number is increased to $T = 200$, the electric force becomes strong enough to induce the formation of two additional convective cells, whose size tends to grow with increasing T up to $T = 500$. Moreover above the value of $T = 300$, the electric force becomes strong enough to distort the mushroom-shaped vortical structure and to form convective cells of more complex shapes, as shown in Figs. 11(d–g).

For $600 \leq T$, the electric forces become strong enough to dominate the flow, leading to the formation of more than two additional convection cells, as shown in Fig. 12. The newly formed cells can interact with each other and give rise to complex flow patterns, such as secondary flows and instabilities, which can lead to asymmetries in the charge density and temperature distributions, as well as in the vortical structure of the domain. At higher values of the electric Rayleigh number, the vortical structure of electro-thermo-convection can become highly turbulent and include a wide range of scales, from large-scale rolls to small-scale eddies. In this regime, the flow patterns can be highly irregular and difficult to predict, and may display features such as intermittent bursts of activity, chaotic behavior, and the formation of localized regions with high vorticity and mixing. A thorough investigation of the above flow features is out of the scope of the current study.

7.3. Enhancement of heat transfer

This section discusses the enhancement of heat transfer from the surface of a hot sphere by imposing the Coulomb force. The heat transfer enhancement by electro-convection is analyzed in terms of the Nusselt number, Nu, defined as the ratio of convective to conductive heat fluxes. In the current study, we focus on the calculation of $\overline{Nu}_c$ and $\overline{Nu}_h$ related to the surfaces of the cold cubic enclosure and the hot sphere, respectively. The calculation of $\overline{Nu}_c$ is based on the arithmetic average of the Nusselt numbers at every wall of the cube as:

$$\overline{Nu}_c = \frac{1}{N}\sum_{i=1}^{N}\overline{\frac{\partial\theta}{\partial \boldsymbol{n}}}, \tag{30}$$

where $\overline{\frac{\partial\theta}{\partial \boldsymbol{n}}}$ refers to the averaged temperature gradient on the surface of given faces of the cubic enclosure, and N is the number of thermally conducting faces. Calculation of $\overline{Nu}_h$, is obtained by accounting for the heat flux from the sphere surface:

$$\overline{Nu}_h = Pr\Delta x\overline{f_\theta}, \tag{31}$$

where $\overline{f_\theta}$ is the average heat flux obtained by an arithmetic mean of all the non-dimensional heat fluxes f_θ^K at each Lagrangian point X^k of the immersed surface. At steady state, the value of the total dimensionless heat flux entering into system from the sphere should be the same as that leaving the cube. The total averaged flux is calculated by multiplying it by the total area of non-insulated cube faces. For the steady state flow, the following condition should be satisfied:

$$4\pi R^2\overline{Nu}_h = 6H^2\overline{Nu}_c. \tag{32}$$

Note also that for the transient flow the values of $\overline{Nu}_c$ and $\overline{Nu}_h$ should also be averaged over a long enough period of time. Fig. 13 depicts the dependence of the $\overline{Nu}_c$ number averaged over the surface of a sphere on the electric Rayleigh number, T. As the Coulomb

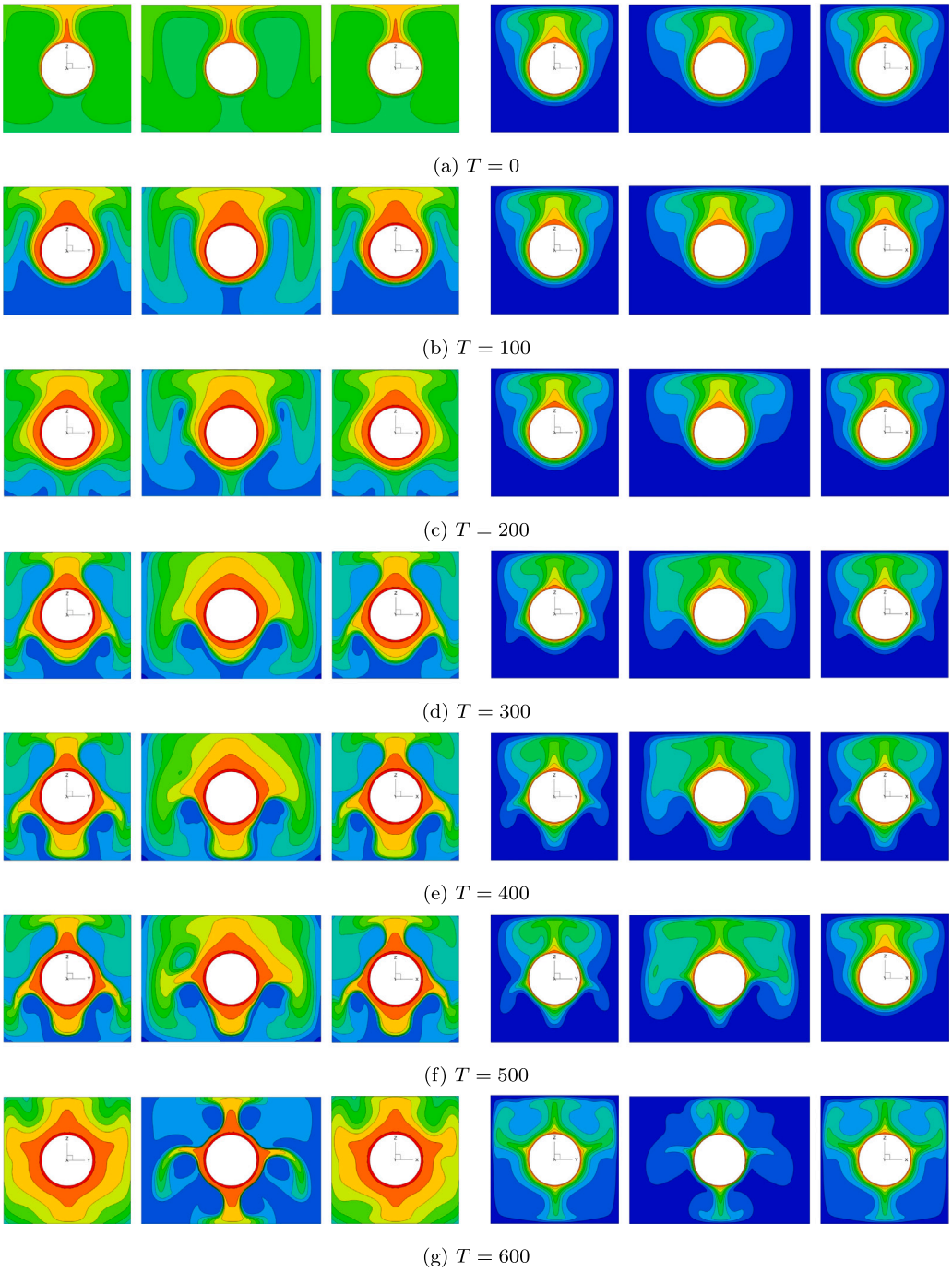

Fig. 9. Distributions of charge density (left 3 columns) and temperature (right three columns) in $Z - Y$, main diagonal, and $Z - X$ cross-sections in transient state. The color palette consists of 10 evenly distributed contours with red color corresponding to $q = 1$, $\theta = 1$ and blue color corresponding to $q = 0$, $\theta = 0$ values.

force becomes stronger (with an increase in T), the electric field induces a radial flow, resulting in an increase in convective heat transfer. The results shown in Fig. 13 can be categorized into two flow regimes. For low T values (ranging from 0 to approximately 250), the heat transfer is dominated by thermal convection, and therefore its variation with T is weak. For higher T values the slope of the $\overline{Nu} - T$ curve increases rapidly at about $T = 300$ and remains approximately constant for higher T values. Note that for the maximal value of $T = 1300$ the $\overline{Nu}_c$ value is higher by a factor of about 3 compared to the configuration characterized by $T = 0$, i.e. when heat transfer is solely driven by the natural convection and conduction. It is noteworthy that in the $3D$ case the dominance

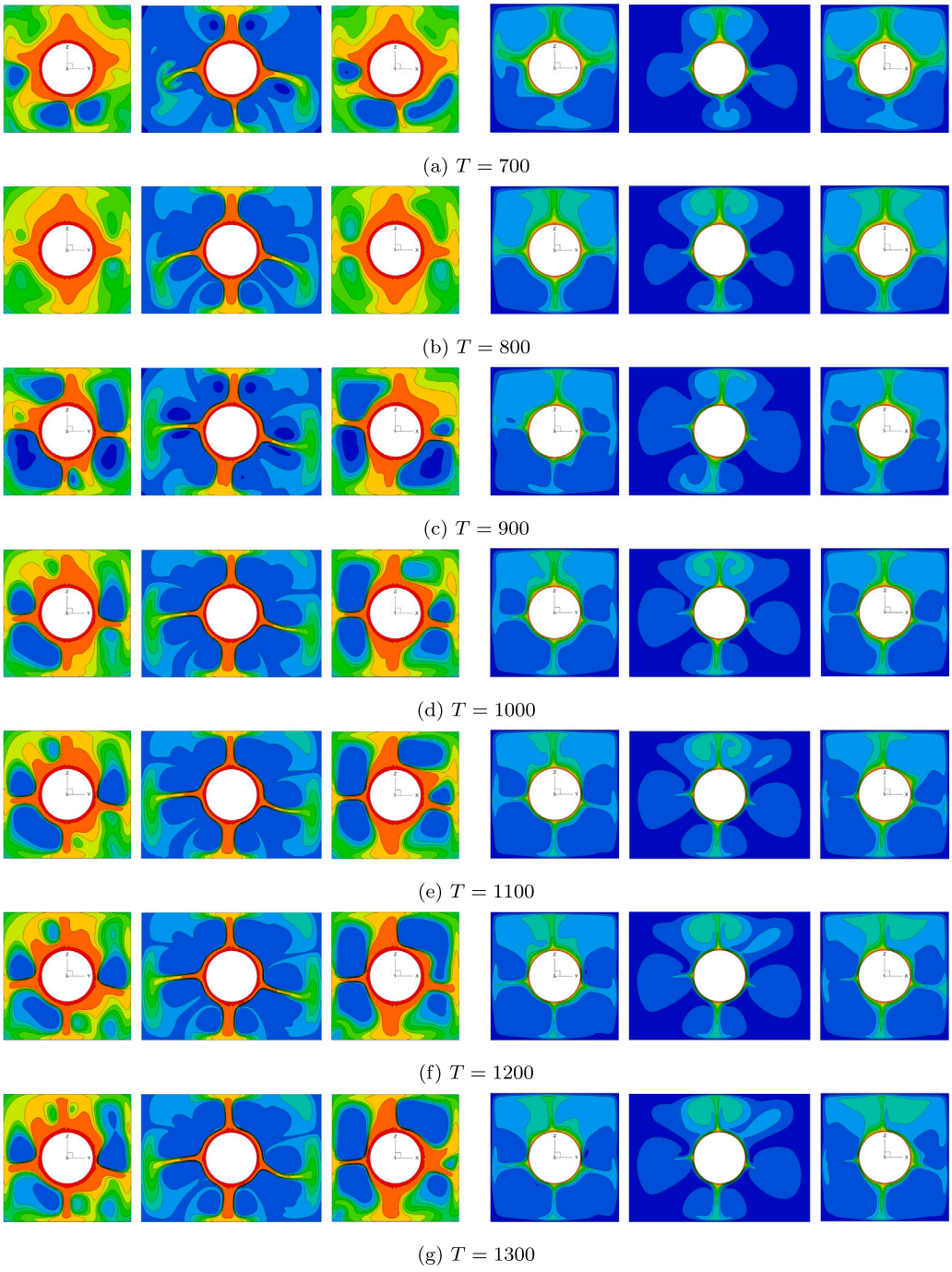

Fig. 10. Distributions of charge density (left 3 columns) and temperature (right three columns) in $Z-Y$, main diagonal, and $Z-X$ cross-sections in transient state. The color palette consists of 10 evenly distributed contours with red color corresponding to $q = 1$, $\theta = 1$ and blue color corresponding to $q = 0$, $\theta = 0$ values.

of electro driven forces over the free convective one is less pronounced compared to its $2D$ counterpart. In fact, with the comparison to the previously reported results related to the natural and electro-convection flows developing in a $2D$ cold square enclosure with a hot circular cylinder placed at its center [51] reveals that about a three fold increase in the Nu number is already achieved at $T = 800$. For the $2D$ counterpart the length of the enclosure side and the diameter of the cylinder are as those used in the current study. The observed difference can be explained by the fact that the $2D$ flow is characterized by a critical threshold value of T above which electro-convection solely controls the flow structure, and the impact of the buoyancy forces becomes negligible. However,

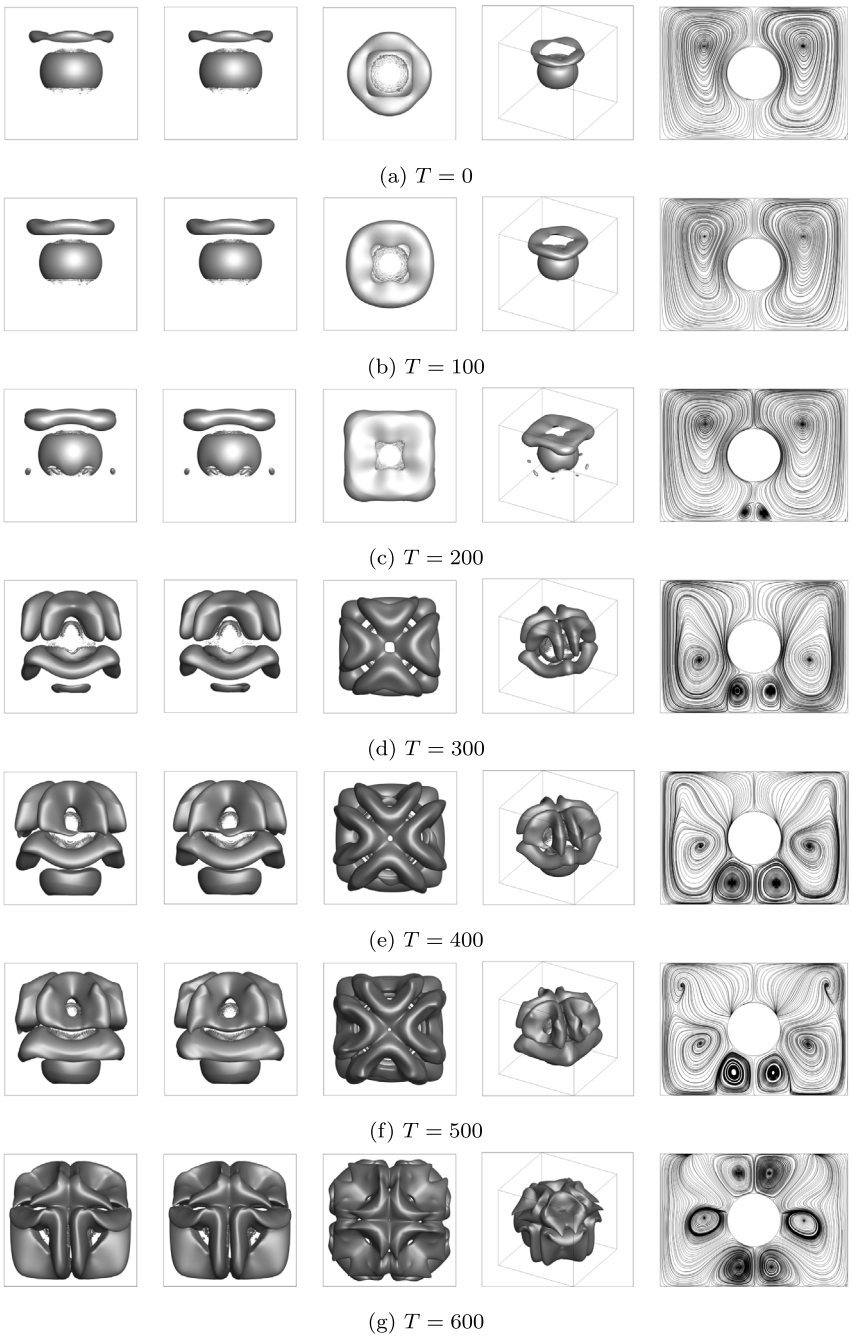

Fig. 11. Vortical structure visualized by the iso-surfaces of $\lambda_2 = -10$ obtained for $Ra = 10^5$ and the range of $0 \leq T \leq 600$. The figures correspond (from left to right) to the λ_2 iso-surfaces taken in $Z-Y$, $Z-X$, $X-Y$ and isometric views and the path lines projected onto the main diagonal plane, respectively.

in the currently investigated fully $3D$ configuration, full dominance of electro-convection is not achieved even at very high (up to 1300) values of T.

8. Conclusions

The current study focusses on the extension of a direct forcing IB method for the simulation of $3D$ electrically driven flows developing around bodies of complex geometry. The developed method has been verified by comparison of the obtained results with data independently obtained for the solution of $1D$ Nernst–Planck equations in radial coordinates in the domain confined by two

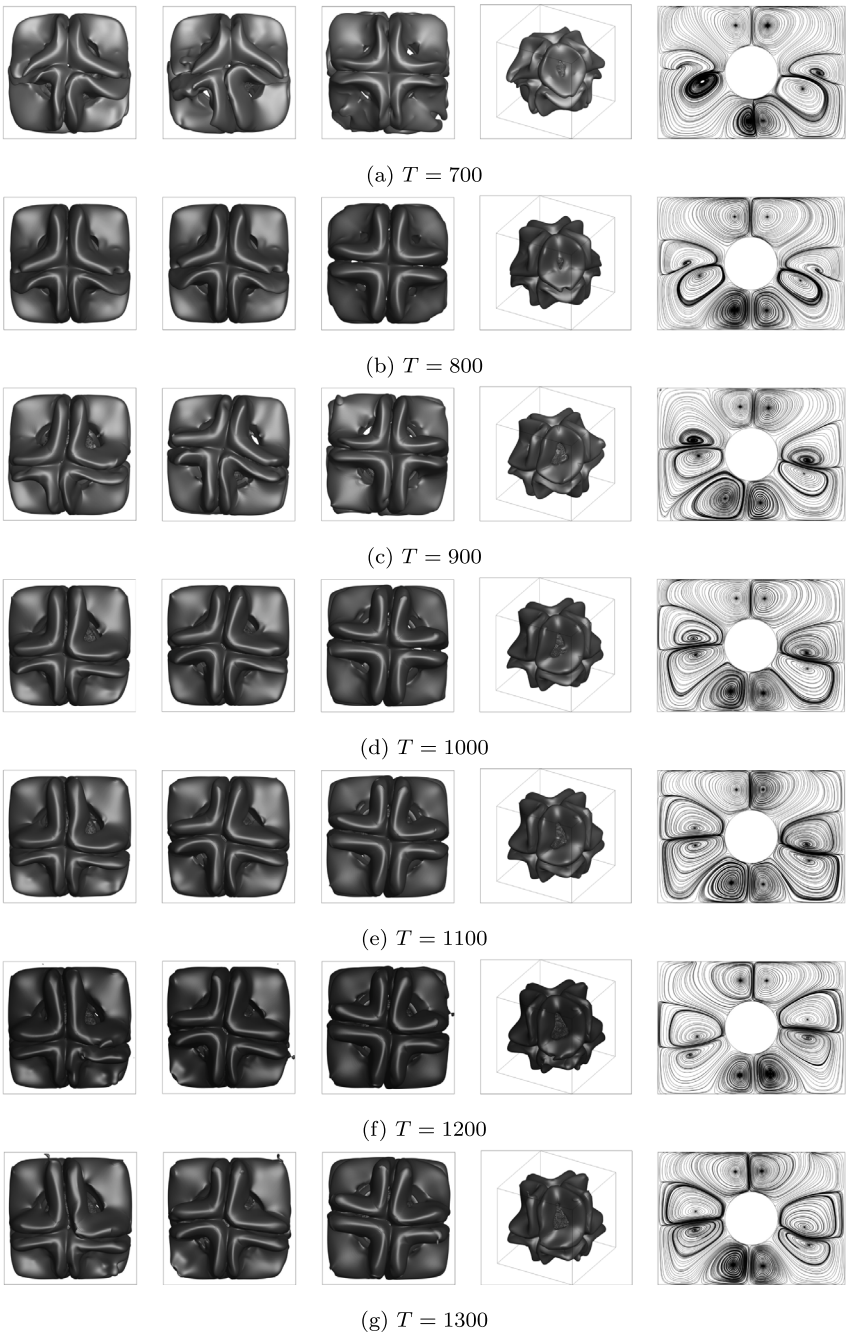

Fig. 12. Vortical structure visualized by the iso-surfaces of $\lambda_2 = -10$ obtained for $Ra = 10^5$ and the range of $700 \leq T \leq 1300$. The figures correspond (from left to right) to the λ_2 iso-surfaces taken in $Z-Y$, $Z-X$, $X-Y$ and isometric views and the path lines projected onto the main diagonal plane, respectively.

concentric ejecting electrodes of spherical shape. The currently developed framework has been verified for its capability to accurately simulate electro-thermo-convection flows. The pseudo-time technique embedded within the direct tensor product factorization (TPF) based solver [38] is employed for the solution of the stationary Poisson equation to meet limitations of memory consumption. This enabled reducing the RAM consumption by nearly 20 times compared to the analogous solution of the purely stationary Poisson equation.

The characteristics of fully $3D$ electro-thermo-convective flow developing around an ejecting hot spherical electrode placed at the center of a cold cubic enclosure are thoroughly investigated. The study confirmed the potential of electro-thermo-convective heat transfer in $3D$ for achieving considerable (about three fold) enhancement in the heat removal rate from the surface of a hot sphere

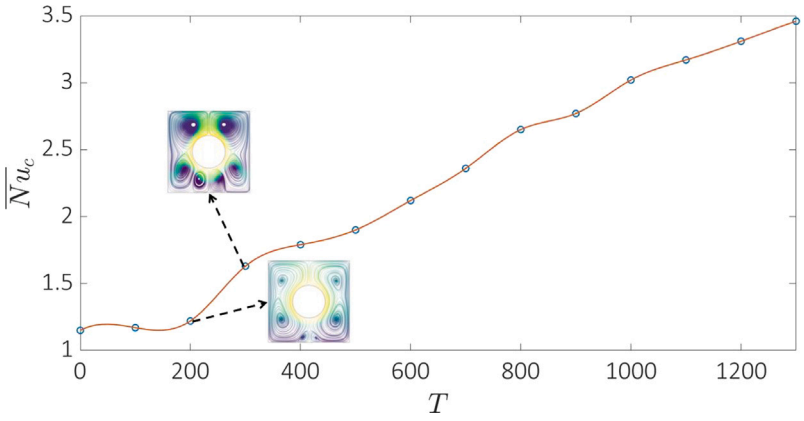

Fig. 13. The dependence of $\overline{Nu_c}$ on electric Rayleigh number T.

compared to the configuration characterized by solely natural convection heat transfer. The differences between steady state and transient characteristics of the considered electro-thermo-convective flow were investigated both qualitatively and quantitatively. The range of the electric Rayleigh number, T, values at which the steady-unsteady transition sets in is determined. Finally, it is revealed that the heat removal characteristics of the considered $3D$ configuration are similar to its corresponding $2D$ counterpart, albeit in $3D$ no critical threshold value of T for the full dominance of electro-convection over natural convection heat transfer has been distinguished.

The current work has been restricted to the investigation of influence of only the electric Rayleigh number, T, on the flow and heat transfer characteristics of the considered flow. A natural continuation of the current study would be to conduct an extensive parametric study of the influence of the mobility number, M, and the injection number, C, on the Nusselt number, which could help in building a comprehensive roadmap allowing further optimization of heat removal from hot ejecting electrodes immersed in a dielectric liquid, and will be the topic of our future work.

CRediT authorship contribution statement

Mukesh Kumar: Writing – original draft, Visualization, Validation, Methodology. **Yohay Mayan:** Visualization, Resources, Methodology, Investigation. **Yuri Feldman:** Writing – review & editing, Visualization, Validation, Supervision, Investigation, Conceptualization.

Declaration of competing interest

The authors declare that they have no known competing financial interests or personal relationships that could have appeared to influence the work reported in this paper.

Acknowledgment

The study is supported by Hewlett Packard Indigo Division Ltd and funded by the Israel Ministry of Energy and Infrastructure (grant No. 315-222-11-049).

Data availability

Data will be made available on request.

References

[1] M. Tański, A. Reza, D.P. a, K. Garasz, A. Tomaszewski, Electrostatic precipitator with surface dielectric barrier discharge ionizer, J. Clean. Prod. 404 (2023) 136990.
[2] L. Pekker, M. Young, Model of ideal electrohydrodynamic thruster, J. Propuls. Power 27 (4) (2011) 786–792.
[3] A. Ratzabi, T. Eluk, A. Levy, Y. Feldman, Nonsymmetric ionic transport in a nonbinary electrolyte at high voltage, Phys. Rev. Fluids 6 (11) (2021) 113701.
[4] M. Ghalamchi, A. Kasaeian, M. Ghalamchi, N. Fadaei, R. Daneshazarian, Optimizing of solar chimney performance using electrohydrodynamic system based on array geometry, Energy Convers. Manage. 135 (2017) 261–269.
[5] P. Traoré, A.T. Pérez, D. Koulova, H. Romat, Numerical modelling of finite-amplitude electro-thermo-convection in a dielectric liquid layer subjected to both unipolar injection and temperature gradient, J. Fluid Mech. 658 (2010) 279–293.

[6] J. Cotton, A. Robinson, M. Shoukri, J. Chang, A two-phase flow pattern map for annular channels under a DC applied voltage and the application to electrohydrodynamic convective boiling analysis, Int. J. Heat Mass Transfer 48 (25) (2005) 5563–5579.
[7] Y. Diao, Y. Liu, J. Zhang, L. Guo, Y. Zhao, S. Wang, Effect of electric field on the enhanced heat transfer characteristic of an evaporator with multilayered sintered copper mesh, J. Electrost. 73 (2015) 26–32.
[8] A. Castellanos, Electrohydrodynamics, vol. 380, Springer Science & Business Media, 1998.
[9] M. Kumar, G. Natarajan, On the role of discrete mass conservation for non-Boussinesq flow simulations in enclosures, Int. J. Heat Mass Transfer 104 (2017) 1283–1299.
[10] F. McCluskey, P. Atten, A. Perez, Heat transfer enhancement by electroconvection resulting from an injected space charge between parallel plates, Int. J. Heat Mass Transfer 34 (9) (1991) 2237–2250.
[11] D. Testi, Heat transfer enhancement by an impinging ionic jet in a viscous transformer coolant, Int. Commun. Heat Mass Transfer 91 (2018) 256–261.
[12] M. Gao, L. shuang Zhang, D. Zhang, L. xin Zhang, Experimental study on the enhancement of free convection heat transfer under the action of an electric field, Exp. Therm Fluid Sci. 104 (2019) 9–14.
[13] W. Grassi, D. Testi, L. Urbanucci, D. Della Vista, Enhanced nucleate boiling and CHF on a small horizontal plate under ionic jet impingement, Int. Commun. Heat Mass Transfer 79 (2016) 67–73.
[14] Y.Y. Yan, H.B. Zhang, J.B. Hull, Numerical modeling of electrohydrodynamic (EHD) effect on natural convection in an enclosure, Numer. Heat Transf. A 46 (5) (2004) 453–471.
[15] J. Wu, P. Traoré, A finite-volume method for electro-thermoconvective phenomena in a plane layer of dielectric liquid, Numer. Heat Transf. A 68 (5) (2015) 471–500.
[16] W. Jian-Zhao, W. Bo-Fu, L. Zhi-Ming, Z. Quan, The heat transfer enhancement by unipolar charge injection in a rectangular Rayleigh–Benard convection, AIP Adv. 12 (1) (2022) 015212.
[17] Y. Wang, G. Qin, W. He, X. Ye, Spectral element method for numerical simulation of ETHD enhanced heat transfer in an enclosure with uniform and sinusoidal temperature boundary conditions, Int. J. Heat Mass Transfer 141 (2019) 949–963.
[18] R.D. Selvakumar, J. Wu, J. Huang, P. Traoré, Electro-thermo-convection in a differentially heated square cavity under arbitrary unipolar injection of ions, Int. J. Heat Fluid Flow 89 (2021) 108787.
[19] J.H. Son, I.S. Park, Numerical investigation of the electro-thermo-convection of dielectric liquid in a square cavity with vertical walls composed of alternately arranged electrodes, Int. Commun. Heat Mass Transfer 129 (2021) 105655.
[20] X. Liang, L. Wang, D. Li, B. Ma, K. He, Lattice Boltzmann modeling of double-diffusive convection of dielectric liquid in rectangular cavity subjected to unipolar injection, Phys. Fluids 33 (6) (2021) 067106.
[21] K. He, Z. Chai, L. Wang, B. Ma, B. Shi, Numerical investigation of electro–thermo-convection with a solid–liquid interface via the lattice Boltzmann method, Phys. Fluids 33 (3) (2021) 037128.
[22] S. Rejeb, W. Hassen, L. Kolsi, P. Estelle, Heat transfer by oil natural convection in an annular space under combined effects of carbon nanotubes and electric field, Int. Commun. Heat Mass Transfer 138 (2022) 106345.
[23] T.-F. Li, X.-R. He, K. Luo, H.-L. Yi, Oscillatory flows of electro-thermo-convection in eccentric annulus, Int. J. Heat Mass Transfer 134 (2019) 920–932.
[24] K. Luo, J. Wu, H.-L. Yi, H.-P. Tan, Numerical investigation of heat transfer enhancement in electro-thermo-convection in a square enclosure with an inner circular cylinder, Int. J. Heat Mass Transfer 113 (2017) 1070–1085.
[25] K. Luo, T. Li, J. Wu, H.-L. Yi, H.-P. Tan, Electro-thermo-convective flow of a dielectric liquid due to nonautonomous injection of charge by an elliptical electrode, Int. J. Heat Mass Transfer 127 (2018) 373–384.
[26] Y. Hu, D. Li, X. Niu, S. Shu, An immersed boundary-lattice Boltzmann method for electro-thermo-convection in complex geometries, Int. J. Therm. Sci. 140 (2019) 280–297.
[27] B. Ma, L. Wang, K. He, D. Li, X. Liang, A lattice Boltzmann analysis of the electro-thermo convection and heat transfer enhancement in a cold square enclosure with two heated cylindrical electrodes, Int. J. Therm. Sci. 164 (2021) 106885.
[28] B. Ma, L. Wang, K. He, D. Li, Electro-thermo-convection in power-law fluids within a square enclosure with an inner cylinder, Phys. Fluids 33 (8) (2021) 083104.
[29] K. Luo, J. Wu, H.-L. Yi, H.-P. Tan, Three-dimensional finite amplitude electroconvection in dielectric liquids, Phys. Fluids 30 (2) (2018) 023602.
[30] Y. Guan, T. Yang, J. Wu, Mixing and transport enhancement in microchannels by electrokinetic flows with charged surface heterogeneity, Phys. Fluids 33 (4) (2021) 042006.
[31] M. Abaszadeh, A. Safavinejad, A. Amiri Delouei, H. Amiri, Analysis of radiative heat transfer in two-dimensional irregular geometries by developed immersed boundary–lattice Boltzmann method, J. Quant. Spectrosc. Radiat. Transfer 280 (2022) 108086.
[32] S. Karimnejad, A.A. Delouei, F. He, Coupling immersed boundary and lattice Boltzmannmethod for modeling multi-body interactions subjected topulsatile flow, Math. Methods Appl. Sci. 46 (2023) 6767–6786.
[33] B. Afra, A.A. Deloue, A. Tarokh, Flow-induced locomotion of a flexible filament in the wake of a cylinder in non-Newtonian flows, Int. J. Mech. Sci. 234 (2022) 107693.
[34] M. Abaszadeh, A. Safavinejad, H. Amiri, A. Delouei, A direct-forcing IB-LBM implementation for thermal radiation in irregular geometries, J. Therm. Anal. Calorim. 20 (2022) 11169–11181.
[35] Y. Feldman, Semi-implicit direct forcing immersed boundary method for incompressible viscous thermal flow problems: a Schur complement approach, Int. J. Heat Mass Transfer 127 (2018) 1267–1283.
[36] C. Chen, Electrohydrodynamic stability, in: A. Ramos (Ed.), Electrokinetics and Electrohydrodynamics in Microsystems, in: CISM Courses and Lectures, vol. 530, Springer, Vienna, 2011, pp. 177–220.
[37] S.V. Patankar, Numerical Heat Transfer and Fluid Flow, CRC Press, 2018.
[38] H. Vitoshkin, A.Y. Gelfgat, On direct inverse of Stokes, Helmholtz and Laplacian operators in view of time-stepper-based Newton and Arnoldi solvers in incompressible CFD, Commun. Comput. Phys. 14 (2013) 1103–1119.
[39] A. Faldun, R. Verzicco, P. Orlandi, J. Mohd-Yusof, Combined immersed-boundary finite-difference methods for three-dimensional complex flow simulations, J. Comput. Phys. 161 (1) (2000) 35–60.
[40] A.M. Roma, C.S. Peskin, M.J. Berger, An adaptive version of the immersed boundary method, J. Comput. Phys. 153 (2) (1999) 509–534.
[41] Y.G. Park, M.Y. Ha, C. Choi, J. Park, Natural convection in a square enclosure with two inner circular cylinders positioned at different vertical locations, Int. J. Heat Mass Transfer 77 (2014) 501–518.
[42] D.B. Stein, R.D. Guy, B. Thomases, Immersed boundary smooth extension (IBSE): a high-order method for solving incompressible flows in arbitrary smooth domains, J. Comput. Phys. 335 (2017) 155–178.
[43] T. Kempe, J. Fröhlich, An improved immersed boundary method with direct forcing for the simulation of particle laden flows, J. Comput. Phys. 231 (9) (2012) 3663–3684.
[44] P. Leopardi, A partition of the unit sphere into regions of equal area and small diameter, Electron. Trans. Numer. Anal. 25 (2006) 309–327.
[45] P. Atten, F. McCluskey, A. Perez, Electroconvection and its effect on heat transfer, IEEE Trans. Electr. Insul. 23 (4) (1988) 659–667.
[46] F. McCluskey, P. Atten, A. Perez, Heat transfer enhancement by electroconvection resulting from an injected space charge between parallel plates, Int. J. Heat Mass Transfer 34 (9) (1991) 2237–2250.

[47] J. Lacroix, P. Atten, E. Hopfinger, Electro-convection in a dielectric liquid layer subjected to unipolar injection, J. Fluid Mech. 69 (3) (1975) 539–563.
[48] J. Jeong, F. Hussain, On the identification of a vortex, J. Fluid Mech. 285 (1995) 69–94.
[49] K. Luo, J. Wu, H.-L. Yi, H.-P. Tan, Lattice Boltzmann model for Coulomb-driven flows in dielectric liquids, Phys. Rev. E 93 (2) (2016) 023309.
[50] N. Felici, J. Lacroix, Electroconvection in insulating liquids with special reference to uni-and bi-polar injection: a review of the research work at the CNRS Laboratory for Electrostatics, Grenoble 1969–1976, J. Electrost. 5 (1978) 135–144.
[51] K. Luo, J. Wu, H.-L. Yi, H.-P. Tan, Numerical investigation of heat transfer enhancement in electro-thermo-convection in a square enclosure with an inner circular cylinder, Int. J. Heat Mass Transfer 113 (2017) 1070–1085.